Autophagy across tissues of aging mice

Authors:

Julian M. Carosi [a,b], Alexis Martin [a], Leanne K. Hein [a], Sofia Hassiotis [a,c], Kathryn J. Hattersley [a], Bradley J Turner [f], Célia Fourrier [a,d], Julien Bensalem [a,d] & Timothy J. Sargeant [a,e]*

Affiliation:

a. Lysosomal Health in Ageing, Lifelong Health Theme, South Australian Health and Medical Research Institute (SAHMRI), Adelaide, South Australia, Australia.
b. School of Biological Sciences, Faculty of Sciences, Engineering and Technology, The University of Adelaide, Adelaide, South Australia, Australia.
c. Current affiliation: Future Industries Institute, University of South Australia, Adelaide, South Australia, Australia.
d. Adelaide Medical School, The University of Adelaide, Adelaide, South Australia, Australia.
e. Faculty of Health and Medical Sciences, The University of Adelaide, Adelaide, South Australia, Australia.
f. The Florey Institute of Neuroscience and Mental Health, University of Melbourne, Parkville, Victoria, Australia.

***Correspondence:**

Tim.Sargeant@sahmri.com

Abbreviations:

CASM; conjugation of ATG8s to single membranes.

PBMCs; peripheral blood mononuclear cells.

PBS; phosphate-buffered saline.

tf-LC3B; tandem fluorescent LC3B/RFP-GFP-LC3B.

Abstract

Autophagy is a ‘waste-disposal’ pathway that protects against age-related pathology. It is widely accepted that autophagy declines with age, yet the role that sex and diet-related obesity play during aging remain unknown. Here, we present the most comprehensive *in vivo* study of autophagic flux to date. We employed transgenic mice overexpressing tandem-florescent LC3B (RFP-GFP-LC3B) to measure autophagic flux in the blood (PBMCs), heart, and motor cortex neurons of aging mice that were fed regular chow or a high-fat diet for 6-, 12- or 18-months. In male mice, aging decreased autophagic flux in the heart, increased it in the blood, and had no effect in motor cortex neurons. Age-dependent changes autophagic flux were less pronounced in female mice. High-fat diet influenced autophagic flux in the blood and heart of male but not female mice. Overall, we uncovered sexual dimorphisms that underpin how autophagy changes with age across different tissues and in response to a high-fat diet.

Introduction

Autophagy captures cytoplasmic components (e.g., damaged organelles, protein aggregates, invading pathogens) within autophagosomes and delivers them to lysosomes for destruction and recycling of their building blocks[1]. This process homeostatically remodels the intracellular environment in response to diverse stimuli[1], and at an organismal level is required for proper fetal development[2,3], adaptation to starvation[4,5], innate immune function[6,7], and prevention of age-related pathologies[8-11].

During autophagy ATG8 homolog proteins (LC3A, -B, -C and GABARAP, -L1 and -L2) are cleaved immediately after a conserved glycine residue in their C-terminus[12], which enables their direct conjugation to lipids on the growing phagophore (LC3B-II refers to its lipidated form)[13,14]. Here ATG8s serve important roles in phagophore maturation[15], the selective capture of substrates (via binding to autophagy cargo receptors)[16] and autophagosome-lysosome fusion[15]. As such, ATG8s are themselves destroyed by the lysosome in an autophagy-dependent manner[17]. LC3B-II levels are a reliable indicator of autophagosome/autolysosome abundance[17,18]. However, 'snapshot' measurements of LC3B-II alone cannot provide information about the rate at which autophagy is occurring (i.e., autophagic flux)[17,18]. Autophagic flux is simple to analyze in cultured cells via measurement of LC3B-II turnover by lysosomes in the presence of lysosome inhibitors (such as bafilomycin, chloroquine, leupeptin)[18], or using LC3B-based probes that report delivery of autophagosomes to lysosomes[19,20], or their lysosome-dependent turnover in the absence of lysosome inhibitors[21].

Critically, measurement of autophagic flux *in vivo* remains challenging. Although it is possible to measure LC3B-II turnover in mice exposed to lysosome inhibitors (such as chloroquine, colchicine, and leupeptin), their tissue distribution is variable and they do not always penetrate the blood-brain barrier[22-27]. Further, because different mice are treated with or without lysosome inhibitors this approach remains a crude estimate of autophagic flux. Moreover, transgenic mice that overexpress GFP-LC3B do not report autophagic flux because GFP fluorescence is lost within acidic autolysosomes, which makes it challenging to uncouple degradation and synthesis of the reporter[28]. pH-sensitive fluorescence allows LC3B-based reporters to track autophagosomes (neutral pH) and autolysosomes (acidic pH), providing a measure of autophagic flux *in vivo* by comparing their abundances (e.g., tandem fluorescent LC3B [tf-LC3B; RFP-GFP-LC3B][29,30] and mKeima-LC3B[31]), or autophagosome degradation relative to synthesis (e.g., GFP-LC3B-RFP-LC3BΔG)[20].

Autophagy limits biological aging and extends lifespan[8-10,32], and it is widely accepted that autophagy declines with age[33]. Indeed, while the degradative capacity of lysosomes is reduced with age in *C. elegans*[34], it remains unclear whether autophagy is affected[35,36]. In

rodents, basal autophagy remains stable in the liver except in extreme old age, while stress-induced proteolysis declines significantly from midlife[37-39]. Autophagic flux was shown to decrease with age in various tissues like liver, heart, kidney, and skeletal muscle, but not white adipose tissue where it increased with age[9,40-42]. Similarly, humans at risk for developing type-2 diabetes show a mild age-dependent increase in autophagic flux within their peripheral blood mononuclear cells (PBMCs)[43].

Aging, diet-related obesity, and sex increase the risk of various age-related diseases affecting the brain and heart. However, it remains unclear if and how these factors interact to influence autophagic flux *in vivo*. Additionally, since PBMCs are useful for measuring autophagic flux in humans[43,44], it is crucial to correlate their flux with that in disease-relevant tissues (e.g., brain and heart). Here, we present the most systematic *in vivo* exploration of autophagic flux to date, revealing how autophagic flux varies across tissues with age and the influence of a high-fat diet, highlighting the differences between sexes.

Results

Measurement of autophagic flux *in vivo* using tf-LC3B

To monitor autophagic flux *in vivo* we employed transgenic mice with tissue-wide overexpression of tf-LC3B[29]. After its cleavage and lipidation, tf-LC3B is incorporated into the phagophore and eventually autophagosome membranes[12-14,19,29,30]. Following autophagosome-lysosome fusion, GFP but not RFP signal from tf-LC3B is quenched by the acidic pH within the autolysosome[19,29,30]. tf-LC3 can therefore distinguish autophagosomes (GFP^+ and RFP^+; i.e., GFP+RFP puncta) from autolysosomes (GFP^- and RFP^+; i.e., RFP-only puncta), which can be used to estimate autophagic flux **(Figure 1A)**[19,29,30]: autophagic flux is high when the number of autolysosomes exceeds that of autophagosomes, and is low when the opposite occurs (Figure 1B)[19,29,30]. A high GFP:RFP ratio indicates that autophagic flux is low, whereas a low GFP:RFP ratio indicates that autophagic flux is high **(Figure 1B)**. Using this approach, we investigated how autophagic flux changed with aging and high-fat diet at 6-, 12-, and 18-months (diet from 2-months of age) for each sex across several tissues including blood (PBMCs) via flow cytometry, or the heart and brain (motor cortex neurons) via confocal imaging **(Figure 1C)**.

We first measured several physiological and metabolic factors to assess how they change with aging and diet for each sex. Mice fed a high-fat diet gained weight quicker than those fed regular chow **(Figure S1A)**. Prior to humane killing, mice were fasted for 6 h prior to sacrifice to reveal blood glucose-related phenotypes on high-fat diet[45]. After 6- and 12-months of age, males but not females were sensitive to high-fat diet-induced changes in their fasting blood glucose levels **(Figure S1B and S1C)**. Moreover, mice fed a high-fat diet displayed a higher incidence of developing liver tumors with age **(Figure S1D and S1E)**.

Autophagic flux increased in an age-dependent manner in the blood

Following extraction from blood, PBMCs from tf-LC3B-expressing mice were analyzed by flow cytometry. We confirmed the presence of monocytes ($F4/80^+$), as well as T- ($CD3^+$), and B lymphocytes ($CD19^+$) in the population gated as PBMCs based on size (FSC-A) and granularity (SSC-A) **(Figure S2A)**. In female mice, autophagic flux in PBMCs was not impacted by a high-fat diet **(Figure 2A)**. Analysis of main-effects indicated that autophagic flux changed with age, but this was difficult to interpret **(Figure 2A)**. Autophagic flux in the PBMCs of male mice strongly increased in an age-dependent manner **(Figure 2B)**. Male mice fed a high-fat diet displayed slightly higher autophagic flux than those fed regular chow at 6-months of age, but this diet effect was not apparent at later time points **(Figure 2B)**. Therefore,

autophagic flux in PBMCs increased with age, but only young males were sensitive to high-fat diet-induced changes.

Autophagic flux decreased in an age-dependent manner in the heart

Next, using confocal microscopy we analyzed how autophagy varied in the heart. In female mice, analysis of main-effects indicated that autophagic flux declined with age, but was not influenced by high-fat diet **(Figure 3A, 3B, S3A and S3B)**. In male mice on a regular chow diet, autophagic flux dropped between 6- and 12-months and continued to decrease by 18-months **(Figure 3C, 3D, S3C and S3D)**. However, in male mice on a high-fat diet, autophagic flux dropped between 6- and 12-months but remained unchanged between 12- and 18-months of age **(Figure 3C, 3D, S3C and S3D)**. By 18 months, male mice fed a high-fat diet had higher autophagic flux than those fed regular chow **(Figure 3C, 3D, S3C and S3D)**. Therefore, an age-dependent decrease in autophagic flux in the heart is modified by high-fat diet in males but not females (**Figure 3A-D)**. These changes do not appear to correlate with expression levels of key autophagy machinery **(Figure S4A and S4B)**.

High-fat diet does not alter autophagic flux in motor cortex neurons

The brain is comprised of heterogeneous cell types including neurons, microglia, astroglia, and oligodendrocytes. Because paraffin embedded brain tissue for immunostaining dulled GFP and RFP signals **(Figure S5A)**, cell-specific markers could not be used to determine how autophagy behaved in each cell type. Instead, we exploited unique morphological features of DAPI-stained nuclei from NeuN$^+$ neurons (i.e., their large size, circular shape, unfilled/ “open” lumen and nucleoli-like inclusions) as a proxy to distinguish neurons in the motor cortex from other cell types such as microglia (IBA1$^+$) or astroglia (GFAP$^+$) **(Figure S5B and S5C)**. Indeed, these characteristics could be reliably employed by a blinded experimenter to distinguish NeuN$^+$ neurons exclusively from their DAPI-stained nuclei morphology, as indicated by receiver operating characteristic curve analysis (AUC = 1) **(Figure S5B and S5C)**. Moreover, because lipofuscin throughout the brain exhibits broad autofluorescence, we excluded GFP$^+$ or RFP$^+$ puncta that were also DAPI$^+$ from our analysis **(Figure S5D and S5E)**. In female mice autophagic flux and SQSTM1/p62-puncta in motor cortex neurons did not change in response to a high-fat diet **(Figure 4A, 4B, S6A, S6B, S7A and S7B)**. Analysis of main-effects indicated that autophagic flux changed with age, but this was hard to interpret **(Figure 4A, 4B, S6A and S6B)**. In male mice autophagic flux and SQSTM1/p62-puncta in motor cortex neurons did not change in response to diet or age **(Figure 4C, 4D, S6C, S6D, S7C and S7D)**. Therefore,

autophagic flux in motor cortex neurons remains relatively stable with aging and in response to a high-fat diet.

Discussion

Our systematic exploration of autophagic flux *in vivo* demonstrates how it changed with age, high-fat diet, and tissue for each sex. In male mice, aging and high-fat diet both modified autophagic flux in the blood (i.e., PBMCs) and heart, but not brain (motor cortex neurons). In female mice, age-dependent changes autophagic flux in motor cortex neurons were complex but statistically significant. In contrast to males, aging exerted milder effects on autophagic flux in the blood and heart of female mice, and was insensitive to dietary modification. This is consistent with the notion that females are protected against several metabolic and physiological consequences of a high-fat diet[46,47]. Although autophagic flux – as an absolute measure – was largely comparable between females and males in the brain and heart, females appeared to have higher autophagic flux in the blood. Autophagy has been reported to be sexually dimorphic in some contexts[48-50], and one plausible explanation for this is that the expression of lysosomal genes and their degradative functions are coordinated by sex hormones and their receptors[51]. Tissue-specific differences in autophagic flux likely reflect differences in their *in vivo* environment[28], sensitivity to stimuli[28], or expression and stoichiometry of components within[52] or upstream of the autophagy pathway[53].

Disabled autophagy is now recognized as a hallmark of aging[33]. Our data support this idea in the heart, but not the brain (motor cortex neurons) or blood (i.e., PBMCs) where autophagic flux did not decrease with age. In contrast, autophagic flux within PBMCs increased in an age-dependent fashion, which is consistent with our recent findings in humans at risk of developing type-2 diabetes[43]. Intriguingly, white adipose tissue also displayed an age-dependent increase in autophagic flux, which is due to reduced expression of the autophagy inhibitor RUBCN[42]. Since PBMCs are currently being used to measure autophagic flux in humans[43,44], it will be important to understand which peripheral organs, tissues or cell-types their flux is correlated with.

Overall, we highlight the importance of considering sex differences and temporal changes when measuring how autophagy behaves *in vivo*.

Limitations of this study

Ratiometric readouts varied depending on tissue complexity or analytical technique used (e.g., puncta per cell [brain], puncta per field of view [heart] and median fluorescence intensity [blood]), meaning that autophagic flux could not be directly compared between tissues. It is plausible that increased autophagic flux in PBMCs might be influenced by age- or diet-related changes to the composition of the PBMC pool (e.g., myeloid skewing)[54]. Critically, by 18-

months of age, mice that were fed a high-fat diet were obese[55] and most developed tumors[56]. This makes it difficult to uncouple whether changes in autophagic flux were due to the diet *per se*, obesity or cancer.

The tf-LC3B probe is useful for monitoring autophagic flux in tissues[19,29,30] but, like all experimental models and approaches, it has drawbacks. The RFP signal of tf-LC3B resists lysosomal degradation and likely over-represents autolysosome abundance and therefore autophagic flux[57]. The GFP:RFP ratio compares the relative abundance of tf-LC3B within non-acidic (i.e., autophagosomes) and acidic compartments (i.e., autolysosomes) at the time of sacrifice. It is therefore a readout for the delivery of autophagosomes to lysosomes, a measure which correlates with – but is not strictly – autophagic flux. The tf-LC3B probe can in rare cases be misleading: for instance, when lysosomes are non-functional yet still acidic[58]. Fluorescent signals from tf-LC3B may also come from non-canonical autophagy pathways (e.g., conjugation of ATG8s to single membranes [CASM])[59]. In some tissues, overexpression of tf-LC3B may lead to autophagy inhibition, such as that seen with GFP-LC3B overexpression[60].

Materials and Methods

Antibodies

Primary antibodies: ATG2B (rabbit polyclonal, PA5-85718, Thermo Fisher); ATG5 (rabbit monoclonal, CST 12994, Cell Signalling Technology); ATG7 (rabbit monoclonal, CST8558, Cell Signalling Technology); ATG13 (rabbit monoclonal, CST 13273, Cell Signalling Technology); ATG16L1 (rabbit monoclonal, CST 8089, Cell Signalling Technology); BECN1 (mouse monoclonal, SC-48341, Santa Cruz); CD3 (clone: 17A2, rat monoclonal-FITC conjugate, CST 86603, Cell Signalling Technology); CD19 (clone: 1D3, rat monoclonal-PE conjugate, CST 82168, Cell Signalling Technology); CTSD (rabbit monoclonal, CST 74089, Cell Signalling Technology); F4/80 (clone: BM8.1, rat monoclonal-VioletFluor450 conjugate, CST 40781, Cell Signalling Technology); FIP200 (rabbit monoclonal, CST 12436, Cell Signalling Technology); GFAP (chicken polyclonal, ab4674, Abcam); GFP (rabbit polyclonal, A-6455, Thermo Fisher) IBA1 (goat polyclonal, ab48004, Abcam); LC3B (rabbit polyclonal, NB100-2220, Novus Biologicals); LMNB1 (rabbit monoclonal, CST 13435, Cell Signalling Technology); NBR1 (rabbit polyclonal, ab126175, Abcam); NeuN (clone: E4M5P, mouse monoclonal, CST 94403, Cell Signalling Technology); NDP52 (rabbit polyclonal, Ab68588, Abcam); SQSTM1/p62 (rabbit polyclonal, PM045, MBL Life Science (imaging) and mouse monoclonal, H00008878-M01, Novus Biologicals (Immunoblotting); ULK1 (rabbit monoclonal, CST 8054, Cell Signalling Technology).

Secondary Antibodies: Alexa Fluor-488 donkey anti-goat IgG (705-545-003; Jackson ImmunoResearch); Alexa Fluor 488 donkey anti-mouse IgG (715-545-151; Jackson ImmunoResearch); Alexa Fluor 647-donkey anti-mouse IgG (715-605-150; Jackson ImmunoResearch); Alexa Fluor 647-donkey anti-rabbit IgG (711-605-152; Jackson ImmunoResearch); Cy3-donkey anti-chicken IgY/IgG (703-165-155; Jackson ImmunoResearch).

Animals

tf-LC3 transgenic mice (C57BL/6-Tg (CAG-RFP/EGFP/Map1lc3b) 1Hill/J; RRID:IMSR_JAX:027139) were kindly provided by Associate Professor Bradley Turner (The Florey Institute, Melbourne, Australia) and a breeding colony was established at the South Australian Health and Medical Research Institute (SAHMRI) following rederivation. Mice were genotyped by genomic PCR of ear notches with the following primers:

F-GFP primer: 5’-CATGGACGAGCTGTACAAGT-3’

R-Map1lc3b: 5’-CACCGTGATCAGGTACAAGGA-3’

F-Internal: 5’-CTAGGCCACAGAATTGAAAGATCT-3’

R-Internal: 5’-GTAGGTGGAAATTCTAGCATCATCC-3’

For this study, 96 tf-LC3 male and female mice (50:50) were randomly assorted to chow (15.6 MJ/Kg, 12.3% total calculated digestible energy from lipids, SF17-091, Specialty Feeds, Australia) or high-fat diet (19.0 MJ/Kg, 43.0% total calculated digestible energy from lipids, SF16-001, Specialty Feeds, Australia) groups from two-months of age. Four additional C57BL/6J (non-transgenic) mice were used as negative controls. Mice were then humanely sacrificed following terminal anesthesia and cardiac puncture after 6-, 12-, and 18-months of age (8 mice/sex/diet at each timepoint). Mice were group-housed (4/cage) in Techniplast individually ventilated cages in a specific and opportunistic pathogen-free facility. Mice were maintained in a controlled temperature room (between 18–24 °C with 45–75% humidity) and a 12 h light/dark cycle (0730–1930 h; UTC+0930). To prevent malocclusion that could be caused by the diet softness, one wood stick was added to every cage. Cage enrichment consisted of two tunnels per cage with sizzle nest and a nestlet. The mice were given *ad libitum* access to food and water. Food consumption was not monitored. Cages were changed twice/week to limit dermatitis that could be caused by the high-fat diet. Food was topped-up twice/week and mice were weighed fortnightly.

All animal experimentation was approved by the SAHMRI Animal Ethics Committee (SAM21-019).

Tissue collection and preparation

Mice were fasted for 6 h, weighed then humanely killed after 6-, 12- and 18-months of age. Mice were culled in the morning by terminal anesthesia using isoflurane and cardiac puncture. Blood glucose was measured using the CONTOUR®NEXT blood glucose monitoring system (Ascensia Diabetes Care Australia). Blood was collected into pre-chilled EDTA tubes and stored on ice before PBMC isolation (see below). Brains were dissected, washed in phosphate-buffered saline (PBS), then sagittally dissected into halves and immersed in 10% neutral buffered formalin (Thermofisher Scientific, Fronine, FNNJJ010). Heart (ventricular muscle) was dissected then washed in PBS and immersed in 10% neutral buffered formalin. One-week after fixation in formalin, tissues were immersed in PBS for one-week before processing.

Confocal microscopy for tf-LC3 mouse tissues

Tissues from the tf-LC3 mice were embedded in 6% low-melt agarose solution (Bio-rad, 1613111) in individual Peel-A-Way embedding cryomolds (Merck) and stored in PBS at 4 °C in the dark until vibratome sections were cut. Tissue slices (40 µm thick) were prepared with

a vibratome (VT1000S, Leica Microsystems) in chilled PBS. Coverslips were mounted onto glass slides with Vectashield antifade mounting media containing DAPI (Vector Laboratories, Abacus DX, H-1200) and sealed with nail polish. Slides were kept at 4 °C in the dark until analysis. Heart and motor cortex sections were imaged at 40× objective with 5× magnification on a Leica TCS SP8X/MP confocal microscope. Images were taken from the same region for each animal for continuity, and focused and imaged using the DAPI channel. The experimenter was blinded to samples throughout imaging and analysis.

Analysis of tf-LC3B puncta to monitor autophagic flux in tissues

GFP^+ and RFP^+ signals from the tf-LC3B probe were quantified in a manner similar to that previously described[61]. Image analysis was performed using FIJI ImageJ.

For the motor cortex, neurons were identified based on $DAPI^+$ nucleus morphology (i.e., based their large size, circular shape, unfilled/ "open" lumen and nucleoli-like inclusions) which reliably identified $NeuN^+$ neurons (confirmed by receiver operating characteristic curve analysis; AUC = 1) (see below). Lipofuscin was identified and excluded if it was observed in the DAPI channel. Each neuronal cell body was traced and saved in the 'ROI manager'. Images were converted to an 8-bit format and then GFP^+ and RFP^+ channels were separated, thresholded, made binary, then puncta were counted within each neuron using the 'analyze particles' function (area = >0.05 μm^2; circularity = 0.00-1.00). GFP^+ and RFP^+ puncta (double positive i.e., autophagosomes) were identified using the 'AND' function of the 'image calculator' then counted within each neuron using the 'analyze particles' function (area = >0.05 μm^2; circularity = 0.00-1.00). GFP^- and RFP^+ puncta (RFP only i.e., autolysosomes) were obtained by subtracting GFP^+ and RFP^+ puncta (double positive i.e., autophagosomes) from the total number of RFP^+ puncta (i.e., autophagosomes and autolysosomes). Then a ratio of autophagosomes:autolysosomes per cell was used to estimate autophagic flux whereby a high autophagosomes:autolysosomes ratio indicates that autophagic flux is low, whereas a low autophagosomes:autolysosomes ratio indicates that autophagic flux is high.

Hearts were analyzed in a similar fashion as motor cortex neurons but with minor differences. Lipofuscin was not detected and therefore did not have to be excluded, and cell boundaries were not traced since individual heart muscle cells were typically longer than the field of view. Therefore, a ratio of autophagosomes:autolysosomes per field of view was used to estimate autophagic flux. In some images, sarcomeres were visible in the GFP channel. However, because their signal was diffuse throughout the cell rather than compact like autophagosomes, they did not interfere with the analysis of GFP^+ puncta after thresholding and particle analysis.

Immunofluorescence

Fixed tissues were paraffin-embedded for microtome sectioning (6 μm thick sagittal sections, rotary microtome; Leica, RM2235) and mounted upon Superfrost Plus Slides (Thermofisher Scientific, Menzel Glaser, SF41296SP). Paraffin sections were dewaxed and rehydrated in xylene and a graded ethanol series prior to microwave antigen retrieval in a 10 mM citrate, 0.05% Tween 20 (pH 6.0) buffer. Sections were blocked (PBS containing 10% normal donkey serum) for 2 h and incubated overnight with primary antibodies diluted in 2% normal donkey serum at room temperature. After washing in PBS, sections were incubated with species-specific fluorophore-conjugated secondary antibody for 2 h, washed, and then mounted with coverslips using VectaShield with DAPI (Vector Laboratories, Abacus DX, H-1200). Slides were kept at 4 °C in the dark until analysis on a Leica TCS SP8X/MP confocal microscope.

Analysis of cell-specific markers and nuclei size in the brain

Motor cortex sections were imaged at 40× objective on a Leica TCS SP8X/MP confocal microscope. Image analysis was performed using QuPath-0.4.4. To test for accuracy of visual identification of neurons using DAPI, the experimenter was first blinded to the cell-type marker channels: neurons (NeuN), microglia (IBA1) and astrocytes (GFAP). Then the DAPI channel was used to identify nuclei that were large, circular, with an unfilled/ “open” lumen with nucleoli-like inclusions (typical of neurons) which were manually selected using the cell counting tool. Following this, channels corresponding cell-type markers were overlayed to verify “true”- and “false”-positives for neuronal nuclei which were counted. Accuracy and sensitivity of this method was determined by receiver operating characteristic curve analysis which yielded an AUC = 1, suggesting it was robust and that nuclei characteristics (large, circular, with an unfilled/ “open” lumen with nucleoli-like inclusions) are a reliable way to identify neurons.

PBMC isolation from tf-LC3 transgenic mouse blood and flow cytometry analysis

Blood samples collected from tf-LC3 mice were used to isolate PBMCs. For each sample tube (~1 mL), cold Dulbecco’s phosphate-buffered saline (DPBS; Gibco, Thermo Fisher Scientific, 14190136) was added to blood (1:1) and samples were mixed by gently pipetting 3–4 times. Four mL of Lymphoprep (Stemcell Technologies, 07811) was added to 10 mL conical centrifuge tubes and the blood/DPBS mixture was carefully overlaid. These tubes were centrifuged for 30 min at 800 × g at 4˚C (with the brake off). PBMCs (white layer at the interface of plasma, upper phase, and Lymphoprep, translucent phase) were carefully aspirated (~2 mL) with a 1 mL pipette and dispensed in a 10 mL conical centrifuge tube. Cold DPBS was added to the PBMCs to a final volume of 6 mL and were mixed gently by inverting tubes 3-4

times. PBMCs were then pelleted by centrifugation at 600 x g for 10 min at 4˚C (with brake on). The supernatant was discarded and the cells were resuspended in 2 mL red blood cell lysis buffer (1X, BD Biosciences, 555,899), mixed by pipetting up-and-down, maintained on ice for 5 min, and mixed again. Five mL of cold DPBS was added and the tubes were centrifuged at 600 x g for 5 min at 4˚C. The supernatant was discarded and the cells were washed one last time in 5 mL cold DPBS and centrifuged at 600 x g for 5 min at 4˚C. The supernatant was discarded and the cells were resuspended in 0.5 mL cold DPBS; the suspension was transferred to a 5 mL tube (Falcon tubes, 5 mL polystyrene; Thermofisher Scientific, 352008) and kept on ice and in the dark before flow cytometry analysis. When required, isolated PBMCs from C57BL/6J (non-transgenic) mice were immunostained for T lymphocyte ($CD3^+$), B lymphocyte ($CD19^+$), and monocyte ($F4/80^+$) markers.

PBMCs were analyzed by flow cytometry on a BD LSR Fortessa X20 Analyser (BD Bioscience, USA). PBMCs were identified based on internal complexity (i.e. granularity; SSC-A) and size (FSC-A) to exclude debris and potential contamination by erythrocytes and granulocytes during the PBMC extraction step. SSC-H versus SSC-A were used to isolate single cells and remove doublets from the analysis. Within this population, GFP and RFP florescence intensities were obtained with BD FACSDiva software (BD Bioscience, USA), similar to that previously described[62,63]. PBMCs from C57BL/6J (non-transgenic) mice served as a background control when analyzing tf-LC3B mice. Median fluorescence intensities (per cell) for GFP and RFP within the PBMC pool were used to calculate GFP:RFP using FlowJo software (Tree Star Inc., Ashland, OR, USA). Importantly, to ensure data consistency over time, the analyser was calibrated at the beginning of each day as per manufacturer's instructions.

Immunoblotting

Hearts were washed in PBS then stored at -80 ˚C. Hearts were homogenised in RIPA lysis buffer, and combined with LDS sample buffer and reducing agent, then proteins were resolved by SDS-PAGE, and transferred onto PVDF membranes. Membranes were blocked for 1 h with 5% skim milk in TBST and probed for indicated proteins overnight at 4 ˚C. Membranes were washed with TBST, probed with HRP-conjugated secondary antibodies for 1 h, re-washed and imaged by chemiluminescence.

Statistical analysis

Graphs and statistical analyses were generated using Prism 10 (GraphPad Software, La Jolla, CA, USA; version 10.2.3). Normal distribution was assessed with the Shapiro-Wilk normality test. Parametric analyses were used for normally distributed data and non-parametric

analyses were used for non-normally distributed data. Figure legends show descriptions of data point values, error bars, statistical tests, and sample size. Results were considered significantly different when $p < 0.05$. Statistically significant p values comparing diet effects are denoted with # symbol; age effects within each diet compared to the 6-month time point are denoted with * symbol; age effects within each diet comparing 12- and 18-month time points are denoted with • symbol; $p < 0.05$ = 1 symbol (i.e., #, * or •); $p < 0.01$ = 2 symbols (i.e., ##, ** or ••); $p < 0.001$ = 3 symbols (i.e., ###, *** or •••); $p < 0.0001$ = 4 symbols (i.e., ####, **** or ••••). We started animal time course experiments with a sample size of n = 8 mice/sex/diet/timepoint. However, several mice died throughout the experiment: one mouse died and three had to be ethically culled due to dermatitis (Figure S1D and S1E). This meant that in some cases <8 mice were analyzed. Moreover, PBMCs were analyzed in <8 mice at the 6-month timepoint due to a flow cytometer breakdown.

Acknowledgements

This investigation was supported by Lysosomal Health in Ageing at SAHMRI, and an Ideas Grant from the National Health and Medical Research Council (GNT2002608) awarded to JB and TJS. JMC is supported by an EMCR Fellowship from The Hospital Research Foundation Group (2022-CF-EMCR-007). The authors acknowledge Microscopy Australia (ROR: 042mm0k03) resources at the Future Industries Institute, University of South Australia, enabled by NCRIS, and thank Dr Sanjna Singh (Lysosomal Health in Ageing at SAHMRI) for experimental advice.

References

1 Kaur, J. & Debnath, J. Autophagy at the crossroads of catabolism and anabolism. *Nat Rev Mol Cell Biol* **16**, 461-472 (2015). https://doi.org/10.1038/nrm4024

2 Yue, Z., Jin, S., Yang, C., Levine, A. J. & Heintz, N. Beclin 1, an autophagy gene essential for early embryonic development, is a haploinsufficient tumor suppressor. *Proc Natl Acad Sci U S A* **100**, 15077-15082 (2003). https://doi.org/10.1073/pnas.2436255100

3 Gan, B. *et al.* Role of FIP200 in cardiac and liver development and its regulation of TNFalpha and TSC-mTOR signaling pathways. *J Cell Biol* **175**, 121-133 (2006). https://doi.org/10.1083/jcb.200604129

4 Kuma, A. *et al.* The role of autophagy during the early neonatal starvation period. *Nature* **432**, 1032-1036 (2004). https://doi.org/10.1038/nature03029

5 Komatsu, M. *et al.* Impairment of starvation-induced and constitutive autophagy in Atg7-deficient mice. *J Cell Biol* **169**, 425-434 (2005). https://doi.org/10.1083/jcb.200412022

6 Zheng, Y. T. *et al.* The adaptor protein p62/SQSTM1 targets invading bacteria to the autophagy pathway. *J Immunol* **183**, 5909-5916 (2009). https://doi.org/10.4049/jimmunol.0900441

7 Thurston, T. L., Ryzhakov, G., Bloor, S., von Muhlinen, N. & Randow, F. The TBK1 adaptor and autophagy receptor NDP52 restricts the proliferation of ubiquitin-coated bacteria. *Nat Immunol* **10**, 1215-1221 (2009). https://doi.org/10.1038/ni.1800

8 Cassidy, L. D. *et al.* Temporal inhibition of autophagy reveals segmental reversal of ageing with increased cancer risk. *Nat Commun* **11**, 307 (2020). https://doi.org/10.1038/s41467-019-14187-x

9 Fernández, Á. F. *et al.* Disruption of the beclin 1–BCL2 autophagy regulatory complex promotes longevity in mice. *Nature* **558**, 136-140 (2018).

10 Pyo, J. O. *et al.* Overexpression of Atg5 in mice activates autophagy and extends lifespan. *Nat Commun* **4**, 2300 (2013). https://doi.org/10.1038/ncomms3300

11 Aman, Y. *et al.* Autophagy in healthy aging and disease. *Nat Aging* **1**, 634-650 (2021). https://doi.org/10.1038/s43587-021-00098-4

12 Tanida, I. *et al.* HsAtg4B/HsApg4B/autophagin-1 cleaves the carboxyl termini of three human Atg8 homologues and delipidates microtubule-associated protein light chain 3- and GABAA receptor-associated protein-phospholipid conjugates. *J Biol Chem* **279**, 36268-36276 (2004). https://doi.org/10.1074/jbc.M401461200

13 Ichimura, Y. *et al.* A ubiquitin-like system mediates protein lipidation. *Nature* **408**, 488-492 (2000). https://doi.org/10.1038/35044114

14 Hanada, T. *et al.* The Atg12-Atg5 conjugate has a novel E3-like activity for protein lipidation in autophagy. *J Biol Chem* **282**, 37298-37302 (2007). https://doi.org/10.1074/jbc.C700195200

15 Nguyen, T. N. *et al.* Atg8 family LC3/GABARAP proteins are crucial for autophagosome-lysosome fusion but not autophagosome formation during PINK1/Parkin mitophagy and starvation. *J Cell Biol* **215**, 857-874 (2016). https://doi.org/10.1083/jcb.201607039

16 Kirkin, V. & Rogov, V. V. A Diversity of Selective Autophagy Receptors Determines the Specificity of the Autophagy Pathway. *Mol Cell* **76**, 268-285 (2019). https://doi.org/10.1016/j.molcel.2019.09.005

17 Kuma, A., Matsui, M. & Mizushima, N. LC3, an autophagosome marker, can be incorporated into protein aggregates independent of autophagy: caution in the interpretation of LC3 localization. *Autophagy* **3**, 323-328 (2007). https://doi.org/10.4161/auto.4012

18 Klionsky, D. J. *et al.* Guidelines for the use and interpretation of assays for monitoring autophagy (4th edition)(1). *Autophagy* **17**, 1-382 (2021). https://doi.org/10.1080/15548627.2020.1797280

19 Kimura, S., Noda, T. & Yoshimori, T. Dissection of the autophagosome maturation process by a novel reporter protein, tandem fluorescent-tagged LC3. *Autophagy* **3**, 452-460 (2007). https://doi.org/10.4161/auto.4451
20 Kaizuka, T. *et al.* An Autophagic Flux Probe that Releases an Internal Control. *Mol Cell* **64**, 835-849 (2016). https://doi.org/10.1016/j.molcel.2016.09.037
21 Yim, W. W., Yamamoto, H. & Mizushima, N. A pulse-chasable reporter processing assay for mammalian autophagic flux with HaloTag. *Elife* **11** (2022). https://doi.org/10.7554/eLife.78923
22 Fourrier, C. *et al.* Comparison of chloroquine-like molecules for lysosomal inhibition and measurement of autophagic flux in the brain. *Biochem Biophys Res Commun* **534**, 107-113 (2021). https://doi.org/10.1016/j.bbrc.2020.12.008
23 Seiliez, I. *et al.* Looking at the metabolic consequences of the colchicine-based in vivo autophagic flux assay. *Autophagy* **12**, 343-356 (2016). https://doi.org/10.1080/15548627.2015.1117732
24 Esteban-Martínez, L. & Boya, P. Autophagic flux determination in vivo and ex vivo. *Methods* **75**, 79-86 (2015). https://doi.org/10.1016/j.ymeth.2015.01.008
25 Ju, J. S., Varadhachary, A. S., Miller, S. E. & Weihl, C. C. Quantitation of "autophagic flux" in mature skeletal muscle. *Autophagy* **6**, 929-935 (2010). https://doi.org/10.4161/auto.6.7.12785
26 Iwai-Kanai, E. *et al.* A method to measure cardiac autophagic flux in vivo. *Autophagy* **4**, 322-329 (2008). https://doi.org/10.4161/auto.5603
27 Haspel, J. *et al.* Characterization of macroautophagic flux in vivo using a leupeptin-based assay. *Autophagy* **7**, 629-642 (2011). https://doi.org/10.4161/auto.7.6.15100
28 Mizushima, N., Yamamoto, A., Matsui, M., Yoshimori, T. & Ohsumi, Y. In vivo analysis of autophagy in response to nutrient starvation using transgenic mice expressing a fluorescent autophagosome marker. *Mol Biol Cell* **15**, 1101-1111 (2004). https://doi.org/10.1091/mbc.e03-09-0704
29 Li, L., Wang, Z. V., Hill, J. A. & Lin, F. New autophagy reporter mice reveal dynamics of proximal tubular autophagy. *J Am Soc Nephrol* **25**, 305-315 (2014). https://doi.org/10.1681/asn.2013040374
30 Castillo, K. *et al.* Measurement of autophagy flux in the nervous system in vivo. *Cell Death Dis* **4**, e917 (2013). https://doi.org/10.1038/cddis.2013.421
31 Hayashi, H. *et al.* Monitoring the autophagy-endolysosomal system using monomeric Keima-fused MAP1LC3B. *PLoS One* **15**, e0234180 (2020). https://doi.org/10.1371/journal.pone.0234180
32 Cassidy, L. D. *et al.* A novel Atg5-shRNA mouse model enables temporal control of Autophagy in vivo. *Autophagy* **14**, 1256-1266 (2018). https://doi.org/10.1080/15548627.2018.1458172
33 López-Otín, C., Blasco, M. A., Partridge, L., Serrano, M. & Kroemer, G. Hallmarks of aging: An expanding universe. *Cell* **186**, 243-278 (2023). https://doi.org/10.1016/j.cell.2022.11.001
34 Sarkis, G. J., Ashcom, J. D., Hawdon, J. M. & Jacobson, L. A. Decline in protease activities with age in the nematode Caenorhabditis elegans. *Mech Ageing Dev* **45**, 191-201 (1988). https://doi.org/10.1016/0047-6374(88)90001-2
35 Chapin, H. C., Okada, M., Merz, A. J. & Miller, D. L. Tissue-specific autophagy responses to aging and stress in C. elegans. *Aging (Albany NY)* **7**, 419-434 (2015). https://doi.org/10.18632/aging.100765
36 Chang, J. T., Kumsta, C., Hellman, A. B., Adams, L. M. & Hansen, M. Spatiotemporal regulation of autophagy during Caenorhabditis elegans aging. *Elife* **6** (2017). https://doi.org/10.7554/eLife.18459

37 Vittorini, S. *et al.* The age-related accumulation of protein carbonyl in rat liver correlates with the age-related decline in liver proteolytic activities. *J Gerontol A Biol Sci Med Sci* **54**, B318-323 (1999). https://doi.org/10.1093/gerona/54.8.b318
38 Donati, A. *et al.* Age-related changes in the regulation of autophagic proteolysis in rat isolated hepatocytes. *J Gerontol A Biol Sci Med Sci* **56**, B288-293 (2001). https://doi.org/10.1093/gerona/56.7.b288
39 Del Roso, A. *et al.* Ageing-related changes in the in vivo function of rat liver macroautophagy and proteolysis. *Exp Gerontol* **38**, 519-527 (2003). https://doi.org/10.1016/s0531-5565(03)00002-0
40 Puleston, D. J. *et al.* Autophagy is a critical regulator of memory CD8(+) T cell formation. *Elife* **3** (2014). https://doi.org/10.7554/eLife.03706
41 Sebti, S., Zou, Z. & Shiloh, M. U. BECN1(F121A) mutation increases autophagic flux in aged mice and improves aging phenotypes in an organ-dependent manner. *Autophagy* **19**, 957-965 (2023). https://doi.org/10.1080/15548627.2022.2111852
42 Yamamuro, T. *et al.* Age-dependent loss of adipose Rubicon promotes metabolic disorders via excess autophagy. *Nat Commun* **11**, 4150 (2020). https://doi.org/10.1038/s41467-020-17985-w
43 Bensalem, J. *et al.* Basal autophagic flux measured in blood correlates positively with age in adults at increased risk of type 2 diabetes. *Geroscience* (2023). https://doi.org/10.1007/s11357-023-00884-5
44 Bensalem, J. *et al.* Measurement of autophagic flux in humans: an optimized method for blood samples. *Autophagy* **17**, 3238-3255 (2021). https://doi.org/10.1080/15548627.2020.1846302
45 Andrikopoulos, S., Blair, A. R., Deluca, N., Fam, B. C. & Proietto, J. Evaluating the glucose tolerance test in mice. *Am J Physiol Endocrinol Metab* **295**, E1323-1332 (2008). https://doi.org/10.1152/ajpendo.90617.2008
46 Oraha, J., Enriquez, R. F., Herzog, H. & Lee, N. J. Sex-specific changes in metabolism during the transition from chow to high-fat diet feeding are abolished in response to dieting in C57BL/6J mice. *Int J Obes (Lond)* **46**, 1749-1758 (2022). https://doi.org/10.1038/s41366-022-01174-4
47 Murtaj, V. *et al.* Brain sex-dependent alterations after prolonged high fat diet exposure in mice. *Commun Biol* **5**, 1276 (2022). https://doi.org/10.1038/s42003-022-04214-x
48 Vega-Naredo, I. *et al.* Sexual dimorphism of autophagy in Syrian hamster Harderian gland culminates in a holocrine secretion in female glands. *Autophagy* **5**, 1004-1017 (2009). https://doi.org/10.4161/auto.5.7.9610
49 Muralimanoharan, S., Gao, X., Weintraub, S., Myatt, L. & Maloyan, A. Sexual dimorphism in activation of placental autophagy in obese women with evidence for fetal programming from a placenta-specific mouse model. *Autophagy* **12**, 752-769 (2016). https://doi.org/10.1080/15548627.2016.1156822
50 Chen, C. *et al.* Apoptosis and autophagy contribute to gender difference in cardiac ischemia-reperfusion induced injury in rats. *Life Sci* **93**, 265-270 (2013). https://doi.org/10.1016/j.lfs.2013.06.019
51 Augereau, P. *et al.* Characterization of the proximal estrogen-responsive element of human cathepsin D gene. *Mol Endocrinol* **8**, 693-703 (1994). https://doi.org/10.1210/mend.8.6.7935485
52 Geng, J., Baba, M., Nair, U. & Klionsky, D. J. Quantitative analysis of autophagy-related protein stoichiometry by fluorescence microscopy. *J Cell Biol* **182**, 129-140 (2008). https://doi.org/10.1083/jcb.200711112
53 Cangelosi, A. L. *et al.* Zonated leucine sensing by Sestrin-mTORC1 in the liver controls the response to dietary leucine. *Science* **377**, 47-56 (2022). https://doi.org/10.1126/science.abi9547

54 Yamamoto, R. *et al.* Large-Scale Clonal Analysis Resolves Aging of the Mouse Hematopoietic Stem Cell Compartment. *Cell Stem Cell* **22**, 600-607.e604 (2018). https://doi.org/10.1016/j.stem.2018.03.013
55 Wang, C. Y. & Liao, J. K. A mouse model of diet-induced obesity and insulin resistance. *Methods Mol Biol* **821**, 421-433 (2012). https://doi.org/10.1007/978-1-61779-430-8_27
56 Bu, L. *et al.* High-fat diet promotes liver tumorigenesis via palmitoylation and activation of AKT. *Gut* **73**, 1156-1168 (2024). https://doi.org/10.1136/gutjnl-2023-330826
57 Katayama, H., Yamamoto, A., Mizushima, N., Yoshimori, T. & Miyawaki, A. GFP-like proteins stably accumulate in lysosomes. *Cell Struct Funct* **33**, 1-12 (2008). https://doi.org/10.1247/csf.07011
58 Mizushima, N., Yoshimori, T. & Levine, B. Methods in mammalian autophagy research. *Cell* **140**, 313-326 (2010). https://doi.org/10.1016/j.cell.2010.01.028
59 Durgan, J. & Florey, O. Many roads lead to CASM: Diverse stimuli of noncanonical autophagy share a unifying molecular mechanism. *Sci Adv* **8**, eabo1274 (2022). https://doi.org/10.1126/sciadv.abo1274
60 Mareninova, O. A. *et al.* Transgenic expression of GFP-LC3 perturbs autophagy in exocrine pancreas and acute pancreatitis responses in mice. *Autophagy* **16**, 2084-2097 (2020). https://doi.org/10.1080/15548627.2020.1715047
61 Carosi, J. M. *et al.* Autophagy captures the Retromer-TBC1D5 complex to inhibit receptor recycling. *Autophagy* **IN PRESS** (2023).
62 Hein, L. K. *et al.* A novel fluorescent probe reveals starvation controls the commitment of amyloid precursor protein to the lysosome. *Biochim Biophys Acta Mol Cell Res* **1864**, 1554-1565 (2017). https://doi.org/10.1016/j.bbamcr.2017.06.011
63 Carosi, J. M. *et al.* Retromer regulates the lysosomal clearance of MAPT/tau. *Autophagy* **17**, 2217-2237 (2020). https://doi.org/10.1080/15548627.2020.1821545

Figure legend

Figure 1. Measurement of autophagic flux *in vivo* using tf-LC3B.

A. Diagram illustrating how tf-LC3B is used to measure autophagic flux in mouse tissues.

B. Diagram illustrating how to interpret autophagic flux as indicated by the tf-LC3B probe.

C. Summary of the experimental workflow for this study.

Figure 2. Autophagic flux increased in an age-dependent manner in the blood.

A. Autophagic flux in female PBMCs. PBMCs extracted from female tf-LC3B mice that were fed regular chow or a high-fat diet for 6-, 12-, and 18-months were analyzed via flow cytometry. Values are GFP/RFP median fluorescence intensity ± sem for n = 4-8 female mice/timepoint (2-way ANOVA).

B. Autophagic flux in male PBMCs. PBMCs extracted from male tf-LC3B mice that were fed regular chow or a high-fat diet for 6-, 12-, and 18-months were analyzed via flow cytometry. Values are GFP/RFP median fluorescence intensity ± sem for n = 4-8 male mice/timepoint (2-way ANOVA with Tukey's multiple comparisons test).

Statistically significant p values comparing diet effects (#); age effects within each diet (coloured) compared to 6-month time point (*) or comparing 12- and 18-month time points (•).

Figure 3. Autophagic flux decreased in an age-dependent manner in the heart

A. Autophagic flux in the female heart. Confocal images of the heart of female tf-LC3B mice that were fed regular chow or a high-fat diet for 6- and 18-months (12-month timepoint not shown). Scale bar: 10 μm. Inset: 10× magnification. Blue on merge: DAPI.

B. Quantification of autophagic flux in the female heart. Values are GFP+RFP/RFP only puncta per field ± sem for n = 6-8 female mice/timepoint (2-way ANOVA).

C. Autophagic flux in the male heart. Confocal images of the heart of male tf-LC3B mice that were fed regular chow or a high-fat diet for 6- and 18-months (12-month timepoint not shown). Scale bar: 10 μm. Inset: 10× magnification. Blue on merge: DAPI.

D. Quantification of autophagic flux in the male heart. Values are GFP+RFP/RFP only puncta per field ± sem for n = 7-8 male mice/timepoint (2-way ANOVA with Tukey's multiple comparisons test).

Statistically significant p values comparing diet effects (#); age effects within each diet (coloured) compared to 6-month time point (*) or comparing 12- and 18-month time points (•).

Figure 4. High-fat diet does not alter autophagic flux in motor cortex neurons

A. Autophagic flux in female motor cortex neurons. Confocal images of the motor cortex of female tf-LC3B mice that were fed regular chow or a high-fat diet for 6- and 18-months (12-month timepoint not shown). Scale bar: 10 μm. Inset: 10× magnification. Blue on merge: DAPI.

B. Quantification of autophagic flux in female motor cortex neurons. Values are GFP+RFP/RFP only puncta per cell ± sem for n = 6-8 female mice/timepoint (2-way ANOVA).

C. Autophagic flux in male motor cortex neurons. Confocal images of the motor cortex of male tf-LC3B mice that were fed regular chow or a high-fat diet for 6- and 18-months (12-month timepoint not shown). Scale bar: 10 μm. Inset: 10× magnification. Blue on merge: DAPI.

D. Quantification of autophagic flux in male motor cortex neurons. Values are GFP+RFP/RFP only puncta per cell ± sem for n = 7-8 male mice/timepoint (2-way ANOVA).

Statistically significant p values comparing diet effects (#); age effects within each diet (coloured) compared to 6-month time point (*) or comparing 12- and 18-month time points (•).

Figure 1

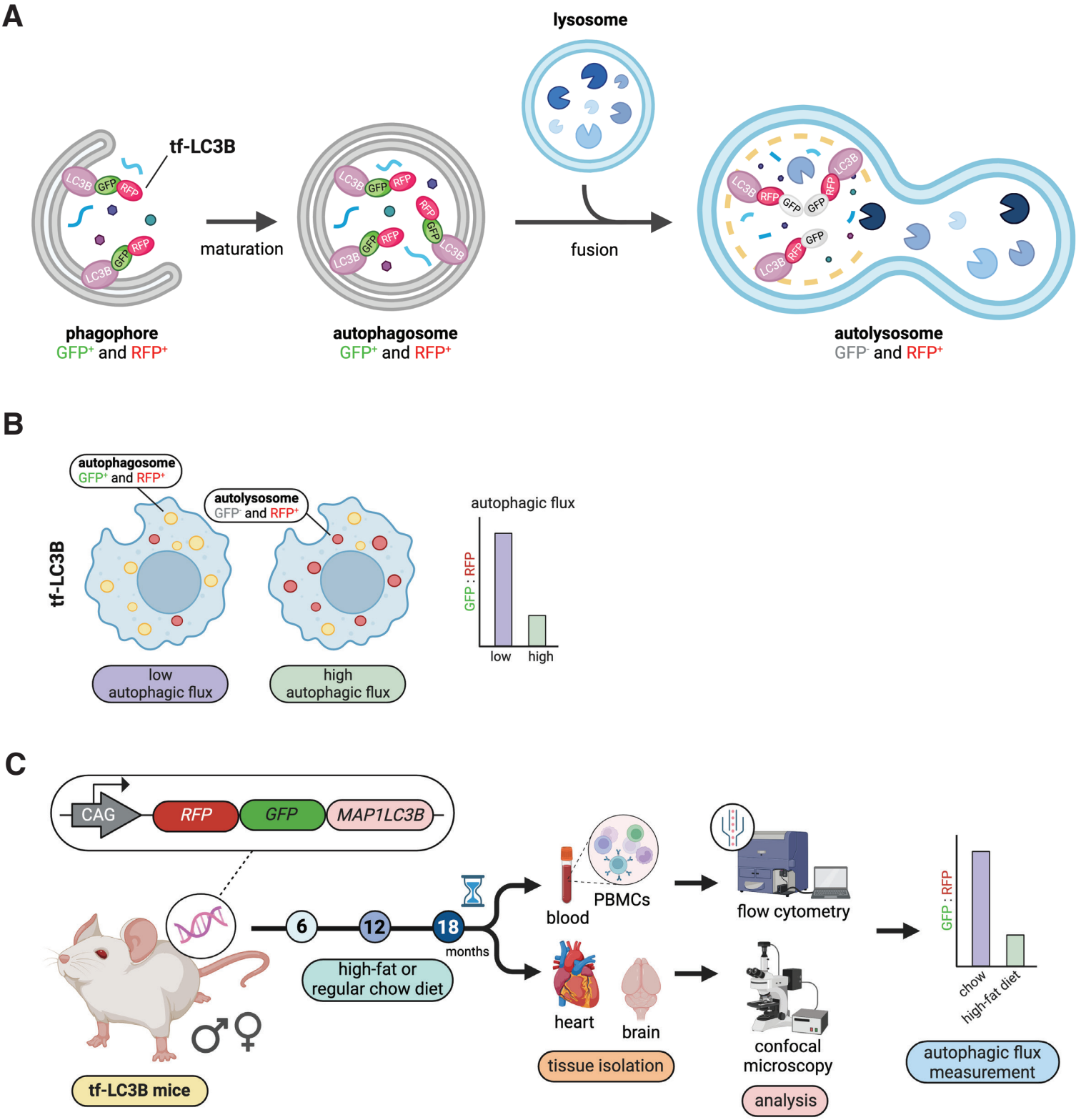
A
lysosome
tf-LC3B
LC3B
GFP
RFP
maturation
fusion
phagophore
GFP+ and RFP+
autophagosome
GFP+ and RFP+
autolysosome
GFP- and RFP+
B
autophagosome
GFP+ and RFP+
autolysosome
GFP- and RFP+
tf-LC3B
low
autophagic flux
high
autophagic flux
autophagic flux
GFP : RFP
low
high
C
CAG
RFP
GFP
MAP1LC3B
6
12
18
months
high-fat or
regular chow diet
tf-LC3B mice
blood
PBMCs
heart
brain
tissue isolation
flow cytometry
confocal
microscopy
analysis
GFP : RFP
chow
high-fat diet
autophagic flux
measurement

Figure 2

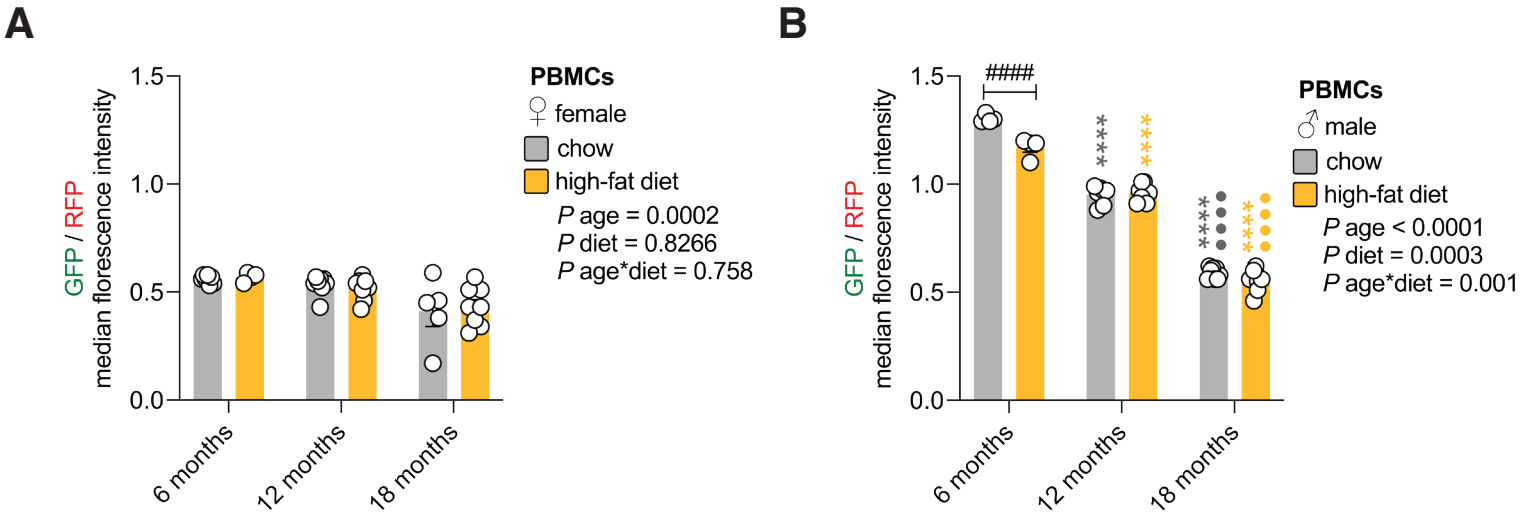
A
GFP / RFP
median florescence intensity
1.5
1.0
0.5
0.0
6 months
12 months
18 months
PBMCs
♀ female
chow
high-fat diet
P age = 0.0002
P diet = 0.8266
P age*diet = 0.758
B
GFP / RFP
median florescence intensity
1.5
1.0
0.5
0.0
####
****
****
****
****
6 months
12 months
18 months
PBMCs
♂ male
chow
high-fat diet
P age < 0.0001
P diet = 0.0003
P age*diet = 0.001

Figure 3

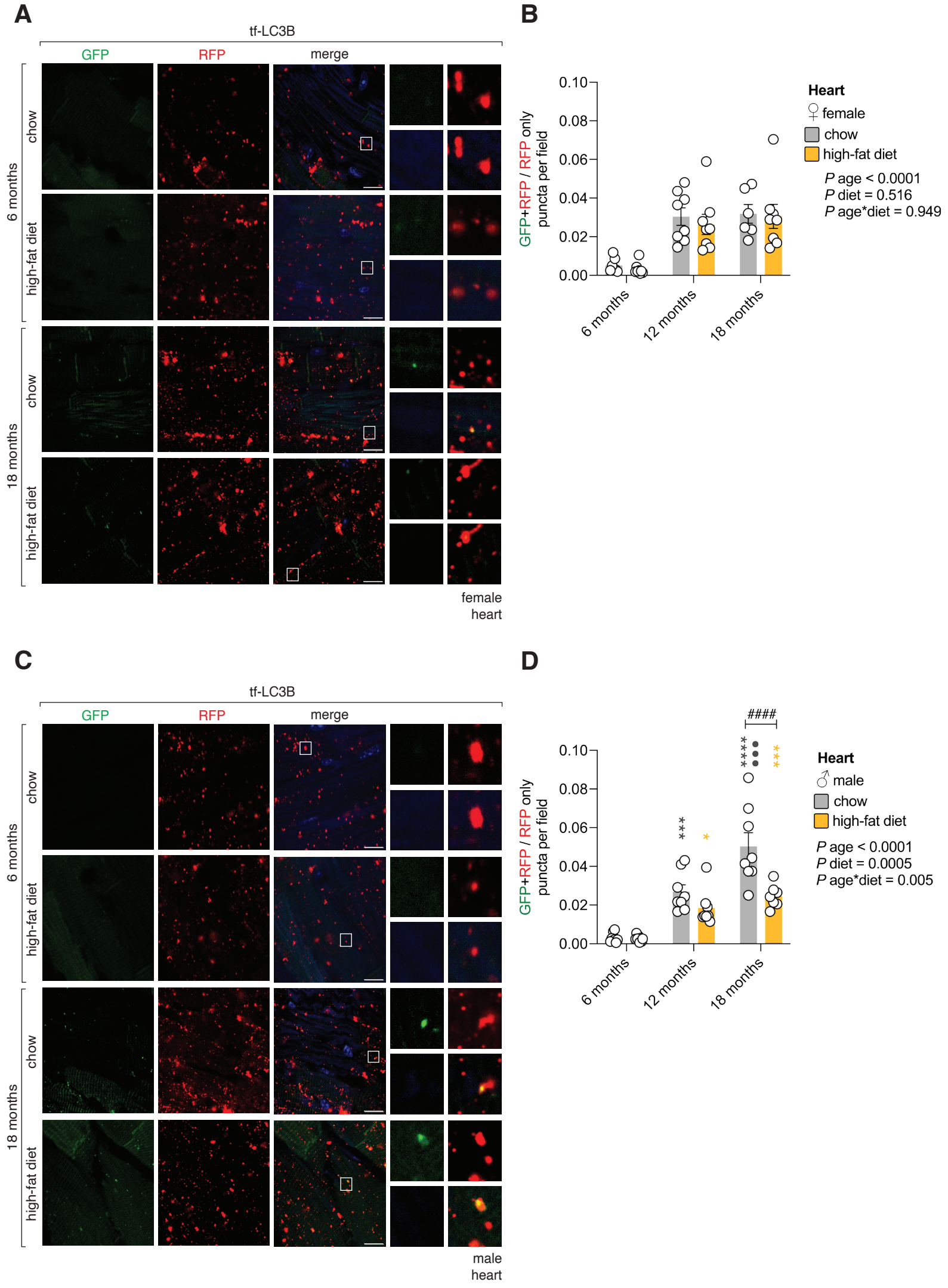
A
tf-LC3B
GFP
RFP
merge
6 months
chow
high-fat diet
18 months
chow
high-fat diet
female heart
B
GFP+RFP / RFP only puncta per field
0.10
0.08
0.06
0.04
0.02
0.00
6 months
12 months
18 months
Heart
female
chow
high-fat diet
P age < 0.0001
P diet = 0.516
P age*diet = 0.949
C
tf-LC3B
GFP
RFP
merge
6 months
chow
high-fat diet
18 months
chow
high-fat diet
male heart
D
GFP+RFP / RFP only puncta per field
0.10
0.08
0.06
0.04
0.02
0.00
6 months
12 months
18 months
***
*
****
***
****
Heart
male
chow
high-fat diet
P age < 0.0001
P diet = 0.0005
P age*diet = 0.005

Figure 4

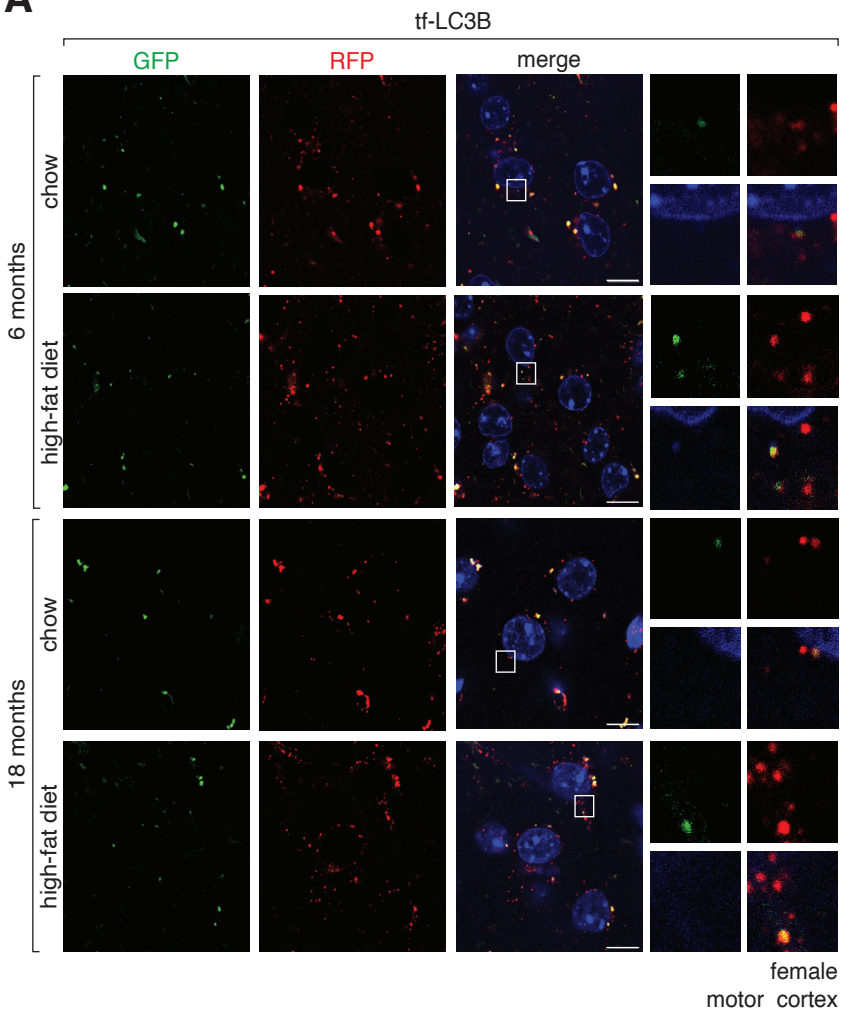
A
tf-LC3B
GFP
RFP
merge
6 months
chow
high-fat diet
18 months
chow
high-fat diet
female
motor cortex

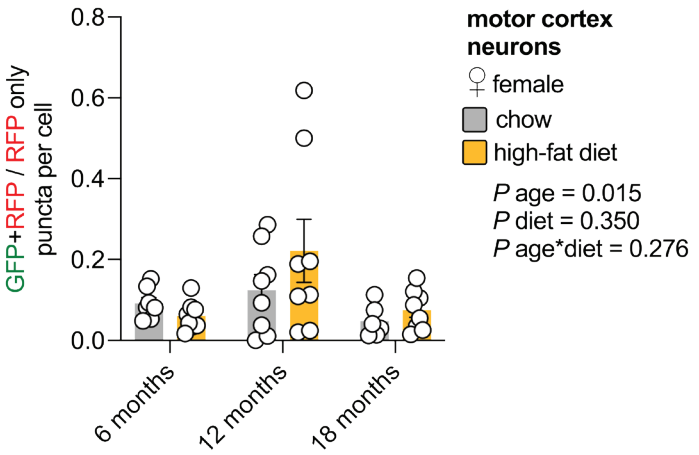
B
GFP+RFP / RFP only
puncta per cell
0.8
0.6
0.4
0.2
0.0
6 months
12 months
18 months
motor cortex
neurons
female
chow
high-fat diet
P age = 0.015
P diet = 0.350
P age*diet = 0.276

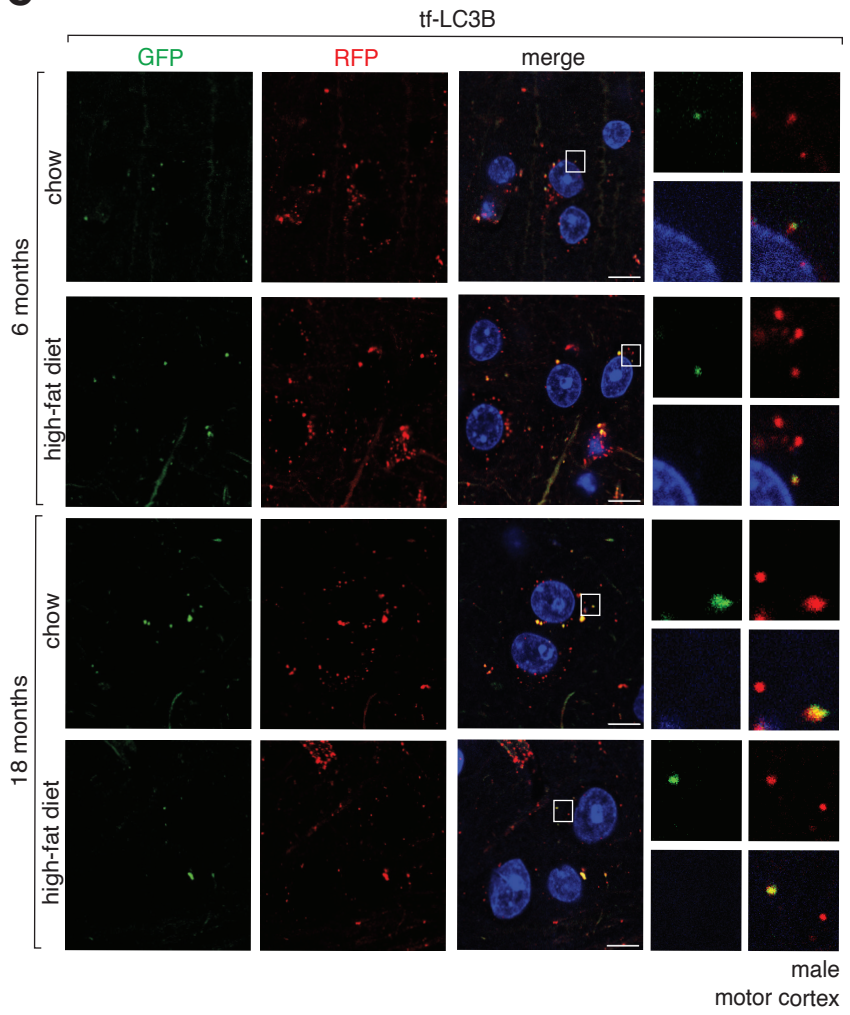
C
tf-LC3B
GFP
RFP
merge
6 months
chow
high-fat diet
18 months
chow
high-fat diet
male
motor cortex

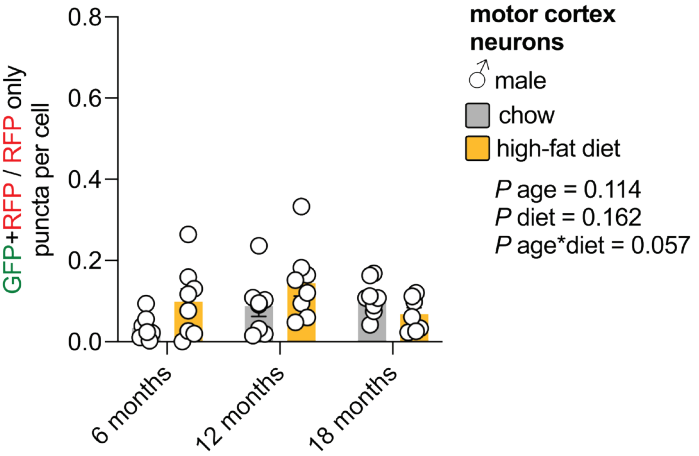
D
GFP+RFP / RFP only
puncta per cell
0.8
0.6
0.4
0.2
0.0
6 months
12 months
18 months
motor cortex
neurons
male
chow
high-fat diet
P age = 0.114
P diet = 0.162
P age*diet = 0.057